Application of randomly oriented spheroids for retrieval of dust particle parameters from multiwavelength lidar measurements

I. Veselovskii,[1] O. Dubovik,[2] A. Kolgotin,[1] T. Lapyonok,[2] P. Di Girolamo,[3] D. Summa,[3] D. N. Whiteman,[4] M. Mishchenko,[5] and D. Tanré[2]

Received 3 March 2010; revised 10 August 2010; accepted 19 August 2010; published 5 November 2010.

[1] Multiwavelength (MW) Raman lidars have demonstrated their potential to profile particle parameters; however, until now, the physical models used in retrieval algorithms for processing MW lidar data have been predominantly based on the Mie theory. This approach is applicable to the modeling of light scattering by spherically symmetric particles only and does not adequately reproduce the scattering by generally nonspherical desert dust particles. Here we present an algorithm based on a model of randomly oriented spheroids for the inversion of multiwavelength lidar data. The aerosols are modeled as a mixture of two aerosol components: one composed only of spherical and the second composed of nonspherical particles. The nonspherical component is an ensemble of randomly oriented spheroids with size-independent shape distribution. This approach has been integrated into an algorithm retrieving aerosol properties from the observations with a Raman lidar based on a tripled Nd:YAG laser. Such a lidar provides three backscattering coefficients, two extinction coefficients, and the particle depolarization ratio at a single or multiple wavelengths. Simulations were performed for a bimodal particle size distribution typical of desert dust particles. The uncertainty of the retrieved particle surface, volume concentration, and effective radius for 10% measurement errors is estimated to be below 30%. We show that if the effect of particle nonsphericity is not accounted for, the errors in the retrieved aerosol parameters increase notably. The algorithm was tested with experimental data from a Saharan dust outbreak episode, measured with the BASIL multiwavelength Raman lidar in August 2007. The vertical profiles of particle parameters as well as the particle size distributions at different heights were retrieved. It was shown that the algorithm developed provided substantially reasonable results consistent with the available independent information about the observed aerosol event.

Citation: Veselovskii, I., O. Dubovik, A. Kolgotin, T. Lapyonok, P. Di Girolamo, D. Summa, D. N. Whiteman, M. Mishchenko, and D. Tanré (2010), Application of randomly oriented spheroids for retrieval of dust particle parameters from multiwavelength lidar measurements, *J. Geophys. Res.*, *115*, D21203, doi:10.1029/2010JD014139.

1. Introduction

[2] Desert dust aerosols play an important role in the Earth's radiation budget [*Moulin et al.*, 1997; *Sokolik et al.*, 2001; *Swap et al.*, 1996]. Dust intrusions can modify the temperature, dynamics and chemical composition of the atmosphere via heterogeneous reactions. To estimate the corresponding radiative forcing, the quantification of size-dependent optical properties of the dust particles is required. Information about the vertical distribution of dust particles both close to a major source region as well as during intrusion episodes has been gained during the last decade by means of elastic-backscatter [*Liu et al.*, 2002, 2008], Raman and high spectral resolution lidars (HSRL) [*Mattis et al.*, 2002; *Müller et al.*, 2003; *De Tomasi et al.*, 2003; *Perrone et al.*, 2004; *Mona et al.*, 2006; *Xie et al.*, 2008]. Raman and HSRL lidars allow an independent calculation of aerosol extinction and backscattering coefficients [*Ansmann et al.*, 1992], together with particle depolarization ratio and are widely used to characterize dust particle properties. For example, much information about dust particle properties was obtained during the Saharan Mineral Dust Experiment (SAMUM) [*Heintzenberg*, 2009; *Ansmann et al.*, 2009; *Esselborn et al.*, 2009; *Freudenthaler et al.*, 2009; *Heese et al.*, 2009; *Tesche et al.*, 2009a; *Wiegner et al.*, 2009]

[1]Physics Instrumentation Center, Troitsk, Russia.
[2]Laboratoire d'Optique Atmospherique, CNRS, Universite de Lille 1, Villeneuve d'Ascq, France.
[3]DIFA, Università della Basilicata, Potenza, Italy.
[4]Mesoscale Atmospheric Processes Branch, NASA Goddard Space Flight Center, Greenbelt, Maryland, USA.
[5]NASA Goddard Institute for Space Studies, New York, New York, USA.

0148-0227/10/2010JD014139

using a unique "lidar park," including Raman and HSRL systems.

[3] The retrieval capabilities of Raman lidars are improved when the measurements are performed at multiple wavelengths. With this information, microphysical properties of aerosols can be retrieved through mathematical inversion [*Müller et al.*, 1999; *Veselovskii et al.*, 2002, 2004]. However, an application of these multiwavelength (MW) algorithms to dust measurements must overcome certain obstacles. For example, all existing lidar algorithms model aerosols as an ensemble of spherical particles even though it is well established that backscattering by irregularly shaped particles is weaker than that predicted by the Mie theory for spheres of equivalent volume. Moreover, lidar backscatter from dust particles is strongly depolarized, thus particle depolarization ratios as high as 30% were observed during SAMUM campaign [*Freudenthaler et al.*, 2009]. The spectral dependence of the particle depolarization ratio contains information about particle parameters, but in the framework of the Mie theory this information cannot be exploited in the retrieval. Therefore, the importance of accounting for particle nonsphericity in lidar retrievals is currently well recognized. However, until now this effect remains underaccounted for in all existing lidar algorithms.

[4] Furthermore, accounting for the effects of particle shape in light scattering is not an issue inherent in lidar techniques only. It is a fundamentally difficult problem that imposes significant limitations on the accuracy of estimates of desert dust aerosol properties with most remote sensing techniques (e.g., see the discussions by *Mishchenko et al.* [2000], *Dubovik et al.* [2006], and *Yang et al.* [2007]). The development of a light scattering model for the retrieval of desert dust properties meets serious obstacles because of the complex nature of the formalism describing light scattering. In situ and laboratory measurements also have issues with sampling of unperturbed aerosols, which complicates the characterization of the particles [e.g., *Bond et al.*, 1999; *Haywood et al.*, 2003; *J. S. Reid et al.*, 2003; *E. A. Reid et al.*, 2003; *Tanré et al.*, 2003]. The optical properties of particles with diverse geometrical shapes and morphologies have been studied for a number of years, but exact solutions describing the interaction of the electromagnetic field with a single particle exist only for several specific geometrical shapes [e.g., *van de Hulst*, 1957; *Bohren and Huffman*, 1983; *Mishchenko et al.*, 2000, 2002]. Existing numerical methods, such as the discrete dipole approximation [e.g., *Draine and Flatau*, 1994] and finite difference time domain technique [e.g., *Yang et al.*, 2000], are more flexible in general, but are very time consuming and in practice can be applied only to particle sizes comparable to and smaller than the wavelength.

[5] To overcome these problems, *Mishchenko et al.* [1995, 1997] suggested to model natural nonspherical aerosol with a mixture of polydisperse, randomly oriented spheroids. In spite the fact that spheroid is the ellipsoid of revolution, a perfectly smooth geometrical form that is obviously far from the actual shape of the real world aerosol particle shape, the spheroid approximation is a clearly appealing concept to account for aerosol particle nonsphericity in lidar applications. First, spheroid is the simplest nonspherical form that generalizes the spherical shape. As discussed in detail by *Mishchenko et al.* [1997] and *Dubovik et al.* [2006] the model of randomly oriented spheroids with only one extra characteristic: the distribution of axis ratios rigorously generalizes the conventional spherical models of atmospheric aerosol (assuming, as the first-order approximation, that shape is independent of size). Correspondingly, for such model, the scattering of electromagnetic radiation can be accurately simulated using the *T*-matrix method by *Mishchenko and Travis* [1994]. This fact assures full consistency of spectral and angular scattering properties of modeled aerosol scattering properties and provides an essential advantage over empirical models of nonspherical aerosol. In addition, a number of studies [e.g., *Wiscombe and Mugnai*, 1986; *Bohren and Singham*, 1991; *Kahnert*, 2004; *Min et al.*, 2005; *Mishchenko et al.*, 1997] show that a mixture of simplified particles (such as spheroids) can successfully mimic properties of real nonspherical aerosol, because exact shape used for modeling is unimportant to a certain degree due to considerable averaging of contributions from individual particles with different orientations, shapes, and compositions.

[6] This concept has been widely employed in numerous applications to account for light scattering effects caused by deviations of particle shapes from that of a sphere. The operational retrieval algorithm employed by the AERONET (Aerosol RObotic NETwork) [*Holben et al.*, 1998] network of ground-based Sun photometers is, perhaps, one of the most vivid examples of using the model of spheroids for the interpretation of aerosol remote sensing observations. First, *Dubovik et al.* [2000, 2002a] used the spheroid model to identify and evaluate the retrieval errors caused by neglecting the effect of particle nonsphericity on AERONET retrievals. More recently, *Dubovik et al.* [2002b, 2006] have developed an approach allowing fast and accurate computations of spheroid ensemble scattering based on precalculated look-up tables of scattering kernels and included the spheroid model in the AERONET retrieval algorithm developed earlier by *Dubovik and King* [2000] in order to account for the shape effects.

[7] More than 5 years of experience with this AERONET code have demonstrated essential improvements in the retrieval of dust properties. First, utilizing the spheroid scattering assumption resulted in the removal of the false fine mode in $dV(r_k)/d\ln r$ and the removal of the false spectral dependence in the real part of the refractive index identified earlier by *Dubovik et al.* [2002a]. Second, utilizing the spheroid model significantly improved accuracy of fitting of desert dust observations by AERONET. Specifically, the spheroid model allowed fitting of the entire angular and spectral set of intensity observations to the level of measurement accuracy, i.e., <5% for sky radiances and <0.01 for aerosol optical thickness. Using the spherical model usually resulted in at least a doubling of the sky radiance fitting error. Detailed discussion of the spheroid model performance in retrieval of Asian aerosols can be found in the studies of *Eck et al.* [2005]. For the case of inverting a new type of AERONET measurements that include spectral and angular measurements of polarization the sensitivity to aerosol particle nonsphericity is even stronger. Results presented by *Dubovik et al.* [2006] illustrate that the spherical assumption results in a 5% residual for the polarization ratio, while using the spheroid model results in a residual below 1%. *Li et al.* [2009] provided more extended analysis of observations by

AERONET Sun photometers with polarimetric capabilities and demonstrated fully satisfactory performance of spheroid based approach for analyzing observations on nonspherical dust.

[8] *Dubovik et al.* [2006] has demonstrated that using spheroid-based models allows identification of all important manifestations of aerosol particle nonsphericity in lidar measurements. It was shown that the spheroid model provides the values of extinction-to-backscatter ratios in the range from ~40 sr to ~75 sr and values of particle depolarization ratio in the range from 10 to 30% for the aerosol with pronounced coarse mode in PSD when Angstrom exponent is less than 1. The mean value of lidar ratio from AERONET obtained by *Cattrall et al.* [2005] based on a spheroid aerosol parameterization was 42 ± 4 sr, which is very close to the observations. Finally, the spheroid-based models of desert dust derived from AERONET retrievals are successfully employed in numerous analyses of satellite-based observations including MODIS [*Levy et al.*, 2007], AVHRR [*Zhao et al.*, 2003], POLDER [*Gérard et al.*, 2005], and MSG/SEVIRI [*Govaerts et al.*, 2010].

[9] Here we adopt the same concept for the incorporation of a spheroidal model into the lidar retrieval of aerosol physical properties. Following the positive experience with the AERONET retrieval development, we model morphologically complex aerosols as a mixture of spherical and nonspherical components, the nonspherical component being an ensemble of randomly oriented spheroids with a size-independent shape distribution. This algorithm is a generalization of our previously published approach [*Veselovskii et al.*, 2002, 2004, 2009] to the retrieval of particle parameters from multiwavelength lidar data. The performance of the algorithm is tested with experimental data from a Saharan dust outbreak episode measured by the BASIL multiwavelength Raman lidar in August 2007.

2. Algorithm Description

2.1. Retrieval Approach

[10] The approach to retrieve the particle microphysical parameters from optical data measured by MW Raman lidar was described in our previous publication [*Veselovskii et al.*, 2002, 2004]. The main features of that algorithm are used here as well. The optical characteristics of an ensemble of polydisperse aerosol particles are related to the particle volume distribution via Fredholm integral equations of the first kind as follows:

$$g_i(\lambda_k) = \int_{\ln r_{\min}}^{\ln r_{\max}} \frac{C_i(m,r,\lambda_k)}{v(r)} \frac{\partial V(r)}{\partial \ln r} d\ln r, i = \alpha, \beta_{\|}, \beta_{\perp}; \quad k = 1, \ldots, n. \tag{1}$$

Here $g_i(\lambda_k)$ describes the optical data at the measurement wavelengths λ_k. The subscript i denotes particle extinction (α) and copolarized ($\beta_{\|}$) or cross-polarized ($\beta_{\perp}$) backscatter coefficients; r is radius of the particle and $v(r)$ is the particle volume. Radii $r_{\min}$ and $r_{\max}$ determine the lower and upper integration limits, $C_i(m, r, \lambda_k)$ denote the extinction and backscattering cross sections, and m is complex refractive index. By using an index p to label the type of optical data (i) and wavelengths λ_k, equation (1) can be rewritten as follows:

$$g_p = \int_{\ln r_{\min}}^{\ln r_{\max}} \frac{C_p(m,r)}{v(r)} \frac{\partial V(r)}{\partial \ln r} d\ln r \quad p = (i, \lambda_k) = 1, \ldots, N_0. \tag{2}$$

[11] A spheroid is a geometrical shape formed by rotating an ellipse about its minor axis (oblate spheroid) or its major axis (prolate spheroid). As was suggested by *Mishchenko et al.* [1997] and *Dubovik et al.* [2006], we assume equal amounts of aspect-ratio-equivalent prolate and oblate spheroids and use the aspect ratio ε (ratio of largest to smallest size) instead of the axis ratio. For example, *Dubovik et al.* [2006] have demonstrated that this assumption does not reduce the ability of the spheroidal mixture to reproduce detailed polarimetric measurements of scattering by mineral dust samples. For the size independent aspect ratio distribution $\frac{dn(\varepsilon)}{d\ln\varepsilon}$, the polydispersion of spheroidal particles can be described using two independent distributions and equation (2) can be rewritten as follows:

$$g_p = \int_{\ln \varepsilon_{\min}}^{\ln \varepsilon_{\max}} \int_{\ln r_{\min}}^{\ln r_{\max}} \frac{C_p(m,r,\varepsilon)}{v(r)} \frac{\partial V(r)}{\partial \ln r} \frac{\partial n(\varepsilon)}{\partial \ln \varepsilon} d\ln r d\ln \varepsilon, \tag{3}$$

or, denoting $K_p(r, m, \varepsilon) = \frac{C_p(r,m,\varepsilon)}{v(r)}$,

$$g_p = \int_{\ln \varepsilon_{\min}}^{\ln \varepsilon_{\max}} \int_{\ln r_{\min}}^{\ln r_{\max}} K_p(r,m,\varepsilon) \frac{\partial V(r)}{\partial \ln r} \frac{\partial n(\varepsilon)}{\partial \ln \varepsilon} d\ln r d\ln \varepsilon. \tag{4}$$

As shown by *Dubovik et al.* [2006], adequate modeling of desert aerosol scattering can be achieved with a $\frac{dn(\varepsilon)}{d\ln\varepsilon}$ not including near-spherical particles with aspect ratios less than ~1.44. Once this condition is satisfied, the retrieval results are generally insensitive to the exact form of $\frac{dn(\varepsilon)}{d\ln\varepsilon}$. Thus, in our model we use a fixed $\frac{dn(\varepsilon)}{d\ln\varepsilon}$ providing the best fit to the detailed polarimetric laboratory measurements for desert dust samples [*Volten et al.*, 2001]. The aspect ratio is varied in the range $1.44 < \varepsilon < 3.0$.

[12] Thus, equation (4) can be written as follows:

$$g_p = \int_{\ln r_{\min}}^{\ln r_{\max}} K_p(r,m) \frac{\partial V(r)}{\partial \ln r} d\ln r, \tag{5}$$

where

$$K_p(r,m) = \int_{\ln \varepsilon_{\min}}^{\ln \varepsilon_{\max}} K_p(r,m,\varepsilon) \frac{\partial n(\varepsilon)}{\partial \ln \varepsilon} d\ln \varepsilon. \tag{6}$$

Representing atmospheric aerosol as a mixture of two fractions: spheres (s) and spheroids (ns), and assuming that the volume fraction of spheroids η is size independent, $\frac{\partial V^{ns}(r)}{\partial \ln r} = \eta \frac{\partial V(r)}{\partial \ln r}$, equation (5) can be rewritten as follows:

$$g_p = \int_{\ln r_{\min}}^{\ln r_{\max}} \left[(1-\eta) K_p^s(m,r) + \eta K_p^{ns}(m,r)\right] \frac{\partial V(r)}{\partial \ln r} d\ln r. \tag{7}$$

Here Kp^s (m, r) and K_p^{ns} (m, r) are the kernel functions for spheres and spheroids, respectively. In order to solve equation (7) numerically, this equation can be transformed into a system of linear equations by approximating the distribution $\partial V(r)/\partial \ln r$ by a linear combination of the base functions $B_j(\ln r)$,

$$\frac{\partial V(r)}{\partial \ln r} \approx \sum_{j=1}^{N_0} \frac{dV(r_j)}{d \ln r} B_j(\ln r). \tag{8}$$

We used the trapezoidal approximation in the ln$r$ space; that is, $B_j(\ln r)$ have triangular shapes with vertices at B_i $(\ln r_{i-1}) = 0$; B_i $(\ln r_i) = \frac{dV(r_i)}{d \ln r}$; B_i $(\ln r_{i+1}) = 0$ (e.g., see details provided by *Dubovik et al.* [2006] and *Veselovskii et al.* [2002]). Equation (7) can be rewritten in a vector–matrix form,

$$\mathbf{g} = [(\eta - 1)\mathbf{A}^s(m) + \eta \mathbf{A}^{ns}(m)]\ \mathbf{C} = \mathbf{A}(\eta, m)\ \mathbf{C}. \tag{9}$$

The optical data are represented by the vector $\mathbf{g} = [g_p]$, and the weight factors by the vector $\mathbf{C} = [\partial V(r_i)/\partial \ln r]$. The matrices $\mathbf{A}^s(m)$ and $\mathbf{A}^{ns}(m)$ consist of the following elements:

$$\left\{A^{s/ns}\right\}_{ij} = \int_{\ln r_{min}}^{\ln r_{max}} K_i^{s/ns}(m, r) B_j(\ln r) d \ln r. \tag{10}$$

Thus, using the system of equation (9) one can find a numerical solution of the integral equation (7). In should be noted that, in principle, the system (9) is nonlinear with respect to all aerosol parameters of our interests, including: $\mathbf{C} = [\partial V(r_i)/\partial \ln r]$ (size distribution), η and m. Therefore, this system can be considered as nonlinear, and solved by iterative procedure searching for the set of C, η and m providing "the best fit" of observations (e.g., AERONET retrieval algorithm by *Dubovik and King* [2000] uses that strategy). Alternatively, using the fact that system of equation (9) is linear in respect of $\mathbf{C}$, one can generate a family of linear solutions for different values η and m and then identify the set $\mathbf{C}$, η and m providing the best fit to the data. Such solution strategy was used in previous work [*Veselovskii et al.*, 2002] and is used here too.

[13] Specifically, for every fixed value of η and m the system of linear equation (9) can be solved via the regularization approach using the well-known expression [*Twomey*, 1977]

$$\mathbf{C} = \left[\mathbf{A}^{\mathrm{T}}(\eta, m)\mathbf{A}(\eta, m) + \gamma \mathbf{H}\right]^{-1} \mathbf{A}^{\mathrm{T}}(\eta, m)\mathbf{g}, \tag{11}$$

where $\mathbf{H}$ is the smoothing matrix of second differences, γ is the regularization parameter, and $\mathbf{A}^{\mathrm{T}}$ is transpose of $\mathbf{A}$. For every set of r_{min}, r_{max}, m_R, m_I, η the solution is found from equation (11). The regularization parameter is determined via minima of modified discrepancy $\rho(\gamma)$ [*Veselovskii et al.*, 2002],

$$\rho(\gamma) = \frac{1}{N_0} \sum_p \left| \frac{g_p - \hat{\mathrm{A}}|f|}{g_p} \right|, \tag{12}$$

where $\hat{\mathrm{A}}$ denotes the integral operator of the Fredholm integral equation (7). We assume that all optical data are measured with the same accuracy, thus their weighting factors in (12) are the same. In our approach we use no a priori information about r_{min}, r_{max} (other that they are inside the interval of 0.05–25 μm), thus we have to consider solutions f_k obtained for different inversion windows (all possible combinations of r_{min}, r_{max}). These solutions for different combinations of m_R, m_I, η are ordered in accordance with their discrepancy ρ_k, from small to large discrepancies. As shown in our previous publications [*Veselovskii et al.*, 2002, 2004], the mean of the solution family obtained by averaging the individual solutions corresponding to small fitting discrepancy generally is close to the "true" solution. To estimate the number of solutions to be averaged it is convenient to consider the dependence of ρ^{av} (discrepancy of averaged solution $f^{\mathrm{av}} = \frac{1}{k}\sum f_k$) on averaging interval ρ_k; that is, we sum the solutions with discrepancy smaller than ρ_k [*Veselovskii et al.*, 2004, 2009]. Typically we average about 1% of total number of solutions and check that the increase of ρ_k does not lead to a significant change in the derived microphysical parameters. Thus, if a sufficient number of independent input data is available, the main particle characteristics such as $\frac{dV(r)}{d \ln r}$, m_R, m_I, η can be retrieved.

2.2. Application of Look-Up Tables of Averaged Kernel Functions to the Retrieval

[14] To solve equation (9), the matrix element $\{A^{s/ns}\}_{ij}$ must be calculated. The software described by *Dubovik et al.* [2006] allows the simulation of the matrix elements $\{A^{s/ns}\}_{ij}$ ("averaged kernels") for any scattering characteristics (scattering, absorption, all elements of scattering matrix for any angle). The kernels were generated in the range of size parameters $0.012 \le x = \frac{2\pi r}{\lambda} \le 625$ using the T-matrix method [*Mishchenko and Travis*, 1994] and the approximate geometric optics integral equation method [*Yang and Liou*, 1996]. A discrete grid of $N_r = 34$ log-equidistant radii r_k, was considered. In the framework of the trapezoidal approximation N_r, triangle base functions $b_k(\ln r)$ centered at r_k were used to generate an "averaged kernel" matrix $\mathbf{K}(m)^{s/ns}$ with the elements.

$$\left\{K(m)^{s/ns}\right\}_{ik} = \int_{\ln r_{k-1}}^{\ln r_{k+1}} K_i^{s/ns}(m, r) B_k(\ln r) d \ln r. \tag{13}$$

[15] The elements of the matrix $K(m)_{ik}^{s/ns}$ for scattering, absorption, copolarized and cross-polarized backscattering were stored into look-up tables. Calculations of light scattering by spherical particles are much less time consuming and could be performed in real time during the retrieval. Nonetheless, for consistency, we use these look-up tables for both spheroids and spherical particles in our algorithm.

[16] As described in section 2.1, the volume distribution $\frac{dV(r)}{d \ln r}$ in our retrieval is approximated by the superposition of triangle base functions $B_j(r)$. The number of these functions is usually 5–8 $\ll N_r$, so for implementation of look-up tables in our program we need to express the base functions $B_j(r)$ through $b_k(r)$ as

$$B_j(r) = \sum_{k=1}^{N_r=34} b_k(r) B_j(r_k).$$

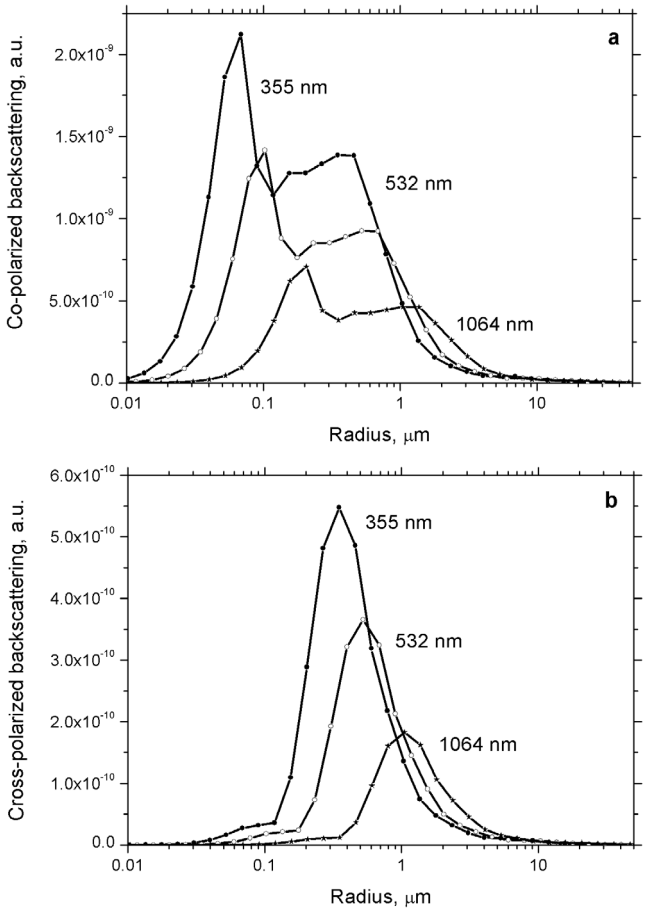

Figure 1. (a) Copolarized and (b) cross-polarized backscattering kernels for spheroids at 355, 532, and 1064 nm wavelengths; m = 1.5−i0.0005.

[17] As we have already mentioned, the minimal and maximal radii of the PSD should be determined in the process of retrieval, thus numerous inversion windows [$r_{\min}$, $r_{\max}$] must be tested. However, N_r = 34 values of r_k are insufficient to cover all the inversion windows and we need to introduce interpolation between r_k to realize this procedure for arbitrary values of $r_{\min}$, $r_{\max}$. It can be done by recalculating look-up table elements $K(m)_{ik}^{s/ns}$ at intermediate radius r'_k inside the interval by using linear interpolation on logarithmic scale,

$$K(m)_{ik'}^{s/ns} \approx K(m)_{ik}^{s/ns} + \frac{K(m)_{ik+1}^{s/ns} - K(m)_{ik}^{s/ns}}{\ln r_{k+1} - \ln r_k}\left(\ln r'_k - \ln r_k\right). \quad (14)$$

The look-up tables were used for inversions within the interval 0.05–25 μm, and the interpolation relationship (14) increases the total amount of inversion windows up to 100, which is sufficient for the retrieval algorithm presented here.

3. Simulation Results

[18] Before applying the developed algorithm to experimental data, an analysis of both the forward and the inverse problem was performed. Studying the forward problem (model) we tried to figure out the difference in input optical data, such as extinction, backscattering and depolarization ratio, when the aerosol is represented by a set of spheres or by a set of randomly oriented spheroids. Analyzing the inverse problem we persuaded to estimate the uncertainties of retrieval for realistic errors in input data and to figure out the uncertainties introduced when particles of irregular shape are treated as spherical.

3.1. Analysis of the Forward Problem

3.1.1. Kernels for Spheres and Randomly Oriented Spheroids

[19] The difference in optical data calculated for the spherical particles and randomly oriented spheroids is determined by the properties of the corresponding kernels in equation (1). For convenience we will note the ith column of matrix $\{K(m)^{s/ns}\}_{ik}$ as $K_i^{s/ns}$, it's elements are averaged kernels at radii r_k, thus the column represents the kernel dependence on particle size. For every chosen wavelength the index i corresponds to different scattering parameters: extinction (α), copolarized, cross-polarized ($\beta_\parallel$, $\beta_\perp$) and total backscattering $\beta = \beta_\parallel + \beta_\perp$. Figure 1 shows spheroidal kernels $K_{\beta_\parallel}^{ns}$, $K_{\beta_\perp}^{ns}$ calculated from equation (13) at 355, 532 and 1064 nm wavelengths and refractive index m = 1.5 −i0.0005. The difference between spherical and spheroidal kernels is illustrated by Figure 2, showing the ratio $\frac{K_\beta^s}{K_\beta^{ns}}$ at λ = 355 nm for different values of imaginary part m_I = 0.0005, 0.005, 0.015; the real part for all curves is m_R = 1.5. The kernels for total scattering are calculated as $K_\beta^{ns} = K_{\beta_\parallel}^{ns} + K_{\beta_\perp}^{ns}$. Up to 0.1 μm the ratio is close to 1, but for larger particles it starts increasing. For big particles (r > 1 μm) the ratio strongly depends on imaginary part m_I: it goes down with m_I increasing and for m_I > 0.015 the spherical and spheroidal kernels approach each other.

[20] Though the size dependence of backscattering kernels for spheres and spheroids is different, the upper boundary of radii interval, where kernels at different wavelengths provide noticeable differences (and can thus be useful for size retrieval), is approximately several micrometers for both types of the particles. The extinction kernels for spheres and

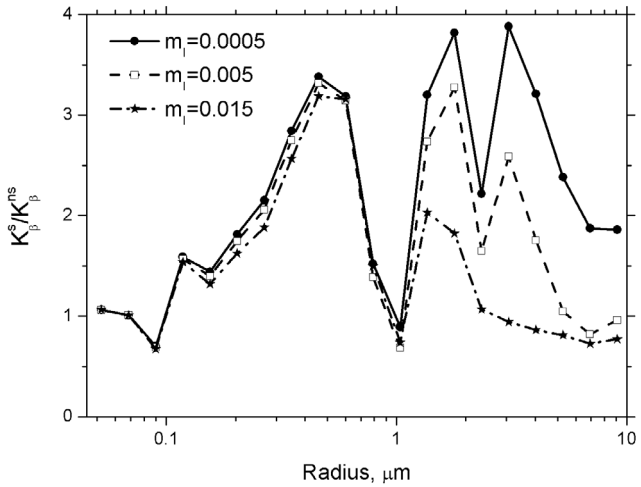

Figure 2. Ratio of spherical to spheroidal backscattering kernels $\frac{K_\beta^s}{K_\beta^{ns}}$ for m_I = 0.0005, 0.005, and 0.015 at λ = 355 nm; m_R = 1.5.

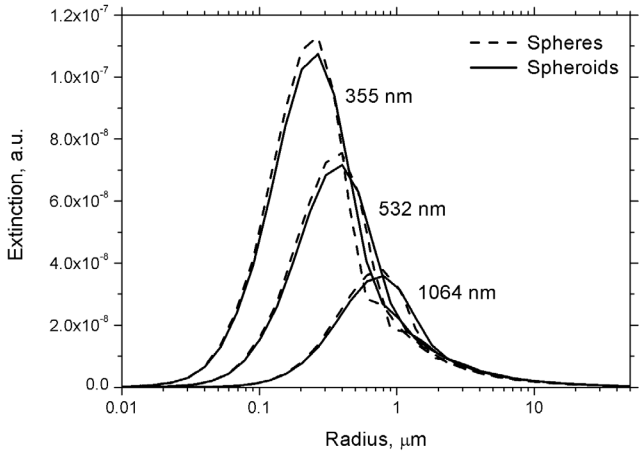

Figure 3. Extinction kernels $K_{\alpha}^{s,ns}$ for spheroids and spheres at 355, 532, and 1064 nm wavelengths; m = 1.5 −i0.0005.

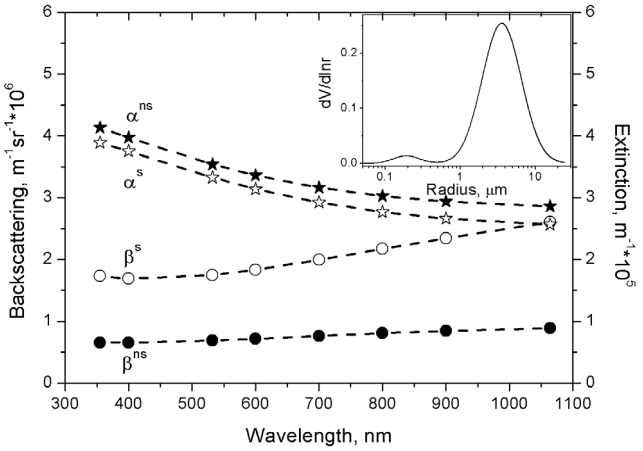

Figure 4. Spectral dependence of the particle backscattering (circles) and extinction (stars) coefficients calculated for spheres (open symbols) and spheroids (solid symbols). The insert shows the PSD_{20} used in calculations; the refractive index is m = 1.55−i0.001; N_f = 100 cm^{-3}.

spheroids shown in Figure 3 practically coincide, and the kernels for cross-polarized backscattering (Figure 1b) also don't extend the retrieval range toward big particles. Thus the radii interval where inversion of optical data with spheroidal kernels is possible should be similar to the interval established previously for spheres [*Veselovskii et al.*, 2004].

3.1.2. Optical Data Computed for Spheres and Randomly Oriented Spheroids

[21] To estimate the difference in optical data for spheres and spheroids we performed the computation of particle extinction and backscattering for a bimodal particle size distribution (PSD),

$$\frac{dn(r)}{d\ln(r)} = \sum_{i=f,c} \frac{N_i}{(2\pi)^{1/2}\ln\sigma_i} \exp\left[-\frac{(\ln r - \ln r_i)^2}{2(\ln\sigma_i)^2}\right]. \qquad (15)$$

Here $N_{f,c}$ is particle number density in the fine (f) and the coarse (c) mode. Each mode is represented by a lognormal distribution with modal radius $r_{f,c}$ and dispersion $\ln\sigma_{f,c}$. In our forward and backward simulations we used two types of size distributions with parameters listed in Table 1. The fine mode has the modal radius $r_f = 0.1$ μm and dispersion $\ln\sigma_f = 0.4$ for both PSDs. To evaluate the effect of particle size on retrieval stability we consider the coarse modes with $r_c = 0.5$ and 0.85 μm, the modal radii for corresponding $\frac{dV}{d\ln r}$ distributions are 2.1 and 3.6 μm. Dispersion of the coarse mode in both cases is $\ln\sigma_c = 0.6$. The maximal particle radii in these distributions are below ~10 μm and ~20 μm correspondingly, so we will call these PSD_{10} and PSD_{20}. The real and imaginary part of refractive index in our simulations varied in the range $1.45 < m_R < 1.55$; $5*10^{-4} < m_I < 0.01$. Long-term worldwide observations in the framework of AERONET demonstrate high variability of dust particles parameters [*Dubovik et al.*, 2002b], nonetheless the values chosen for $r_{f,c}$, $\ln\sigma_{f,c}$ and m are quite representative and may be used to illustrate the main features of the forward and inverse problems.

Table 1. Parameters of Bimodal PSDs Used in the Numerical Simulations

Size Distribution	r_f, μm	$\ln\sigma_f$	r_c, μm	$\ln\sigma_c$	N_f/N_c
PSD_{20}	0.1	0.4	0.85	0.6	100
PSD_{10}	0.1	0.4	0.5	0.6	100

[22] The spectral dependences of particle backscattering and extinction for spheres and spheroids are shown in Figure 4; the PSD_{20} used in computations is given in Figure 4 as insert. For this size distribution the backscattering by spheres more than twice exceeds the corresponding value for spheroids, while extinction for spherical particles is about 10% lower. The lidar ratio at 532 nm is 51 sr for spheroids, which is a typical number for desert dust particles [*Tesche et al.*, 2009a], while for spheres the lidar ratio is only 19 sr.

[23] The input optical data are strongly influenced by the complex refractive index. The dependence of backscattering ($\beta^{s,ns}$) and extinction ($\alpha^{s,ns}$), coefficients on real part of refractive index for PSD_{20} is given by Figure 5. Particles backscattering is enhanced when m_R increases, but β^s rises faster than β^{ns}. The reason for this is the peaking of the spherical phase function in the backward direction (for spheroids the phase function at large scattering angles is flat), and the backward peak rises with m_R. Extinction coefficients for both particle types don't show strong sensitivity to variations in m_R: changing m_R from 1.35 to 1.65 leads to an increase of α^{ns} by 25%, thus the rise of backscattering with m_R leads to a decrease of the lidar ratio.

[24] The dependence of optical data on imaginary part of refractive index is illustrated by Figure 6. In the range of $0.0001 < m_I < 0.02$ the particle extinction shows very little dependence on m_I. At the same time, backscattering decreases fast with m_I and this effect is especially significant for spheres. In the range of m_I variation being considered, β^s decreases by a factor of 5 while β^{ns} decreases by a factor of 3. This difference is again explained by the peaking of phase function for spheres in the backward direction: the peak disappears with m_I increasing and backscattering for spheres and spheroids become close. From Figures 5 and 6

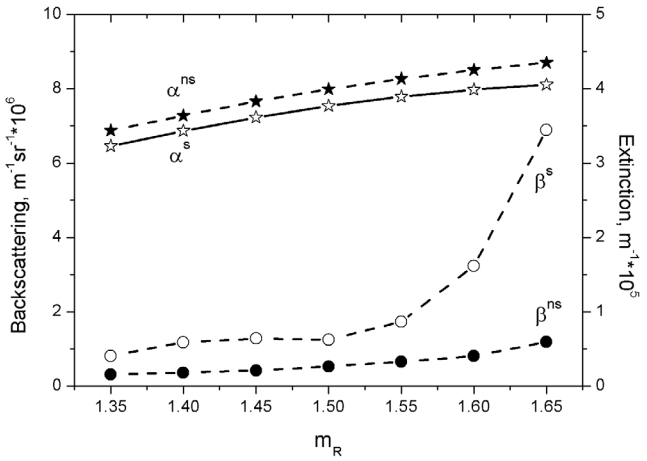

Figure 5. Particle backscattering (circles) and extinction (stars) coefficients at 355 nm wavelength as a function of the real part of refractive index. Calculations for spheres (open symbols) and spheroids (solid symbols) were performed for PSD_{20} with $m_I = 0.001$, $N_f = 100$ cm^{-3}.

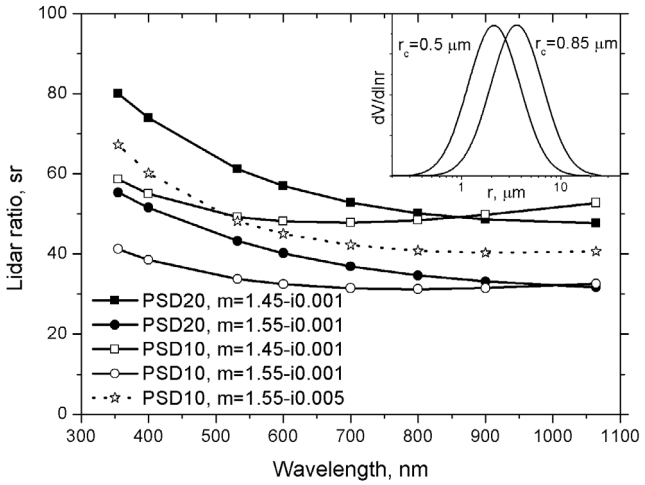

Figure 7. Spectral dependence of the lidar ratio computed for the coarse modes of PSD_{10} and PSD_{20} of spheroids. Calculations were performed for $m_R = 1.55$ and 1.45 and $m_I = 0.001$ and 0.005.

we can conclude that the most significant difference in backscattering of spheres and spheroids occurs for high values of real part and low values of imaginary part of refractive index.

[25] It is important to evaluate the spectral dependence of the lidar and depolarization ratios, because these parameters are becoming available from multiwavelength Raman and HSRL lidars in dust source regions. For example, the results obtained by *Tesche et al.* [2009a] during SAMUM demonstrate that the dust lidar ratio is about 55 sr at 355, 532 and 1064 nm. The depolarization ratio measured by *Freudenthaler et al.* [2009] is about 30% and also does not reveal significant variations in the same spectral range. Thus the comparison of model spectral dependences with experimental results can be an important step in the validation of the ability of a model based on randomly oriented spheroids to represent scattering characteristics of atmospheric dust particles [*Wiegner et al.*, 2009]. The spectral behavior of the lidar ratio is sensitive to the particle size distribution and complex refractive index, so for such a comparison the accurate knowledge of these parameters is required. This detailed comparison is beyond the scope of this paper. The limited purpose of the examples given here is to illustrate the influence of the PSD and refractive index on spectral variations of the lidar and the depolarization ratio and to show that modeled spectral dependences are in qualitative agreement with experimental observations.

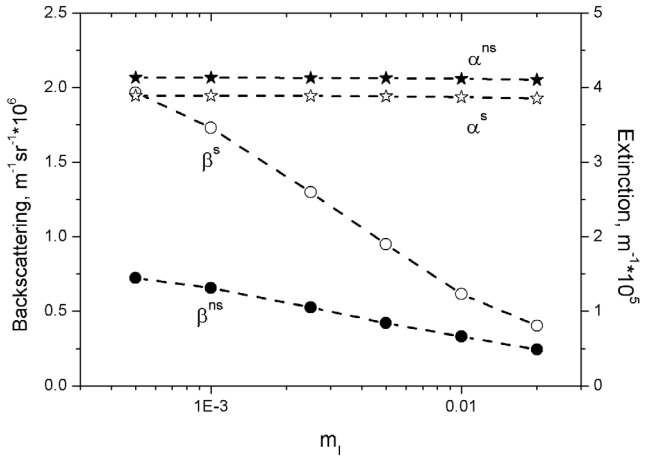

Figure 6. The particle backscattering (circles) and extinction (stars) coefficients at 355 nm wavelength as a function of the imaginary part of the refractive index. Calculations for spheres (open symbols) and spheroids (solid symbols) were performed for the PSD_{20} with $m_R = 1.55$, $N_f = 100$ cm^{-3}.

[26] Figure 7 shows the spectral variation of the particle lidar ratio for different PSDs and refractive indices. The dust particle size distribution in the source region is represented mainly by the coarse mode, and so computations were performed only for the coarse modes PSD_{10} and PSD_{20}, the corresponding size distributions being depicted as inserts in Figure 7. To illustrate the effect of the refractive index, the spectral dependences are shown for m = 1.55–i0.001, 1.45–i0.001, 1.45–i0.005. For the PSD_{20} (m = 1.55–i.001), the lidar ratio decreases with wavelength from 55 sr to 31 sr. For the PSD_{10} and the same refractive index, the spectral dependence flattens: the lidar ratio varies within the range 41 to 32 sr. The decrease of m_R from 1.55 to 1.45 makes the lidar ratio almost spectrally independent and its value increases up to ~55 sr. An increase of the imaginary part enhances the lidar ratio at shorter wavelengths. However, this effect becomes less pronounced with decreasing particle size. It should be noted that the Angstrom exponent calculated at 355–532 nm wavelengths for PSD_{10} is negative (about −0.05), while the Angstrom parameters observed by *Tesche et al.* [2009a] varied in the 0.2–0.4 range, thereby indicating the presence of smaller particles during their observations. This can be one of the factors explaining the weak spectral dependence of the lidar ratio in their measurements.

[27] The spectral behavior of the depolarization ratio computed for the coarse mode PSD_{20} is shown in Figure 8.

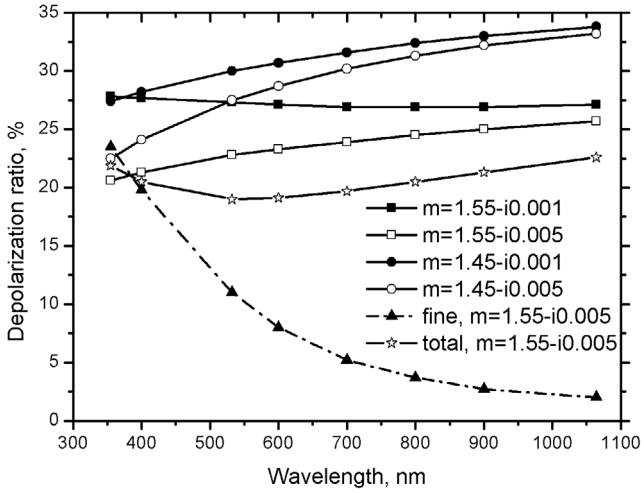

Figure 8. Spectral dependence of the particle depolarization ratio computed from the coarse (circles and squares), the fine (triangles) mode and for total (stars) distribution PSD_{20}. Calculations were performed for refractive indices with m_R = 1.45 and 1.55 and m_I = 0.001 and 0.005.

For m = 1.55–i0.001 the depolarization ratio is about 27% and is spectrally independent. The increase of the imaginary part up to m_I = 0.005 leads to a decrease of depolarization at shorter wavelength (δ_{355} = 20.5%), but the depolarization at 1064 nm hardly changes. For m = 1.45 the depolarization is enhanced, reaching a maximal value of 33% at 1064 nm. For comparison, Figure 8 also shows the spectral dependence of depolarization computed for the fine mode and for the total PSD_{20} with m = 1.55–i0.005. For the fine mode, the depolarization ratio decreases from 24% at 355 nm to 2% at 1064 nm, and thus the resulting spectral dependence of depolarization for the total PSD_{20} is weak. From the curves presented in Figure 8, we can conclude that the spectral variation of the depolarization ratio is in a reasonable agreement with observational data.

3.2. Analysis of Inverse Problem

3.2.1. Retrieval of Parameters of Irregularly Shaped Particles Using Spheroidal and Spherical Kernels

[28] In the analysis of the inverse problem the randomly oriented spheroids with PSD_{10} and PSD_{20} distributions were used to generate the optical data (α, β, ρ). As discussed in section 3.1, such set of spheroids can model the optical data from irregular shape particles with the same $\frac{dV}{d\ln r}$ distribution. In the retrieval both spheroidal and spherical kernels were used. The simulation was performed for a relatively simple (and thus the most widespread) version of MW Raman lidar system based on a tripled Nd:YAG laser. This system provides three backscattering coefficients at 355, 532 and 1064 nm and two extinction coefficients at 355 and 532 nm, the so-called $3\beta + 2\alpha$ configuration. For the purpose of dealing with irregular particles, the particle depolarization ratios δ at three wavelengths in principle are also available.

[29] The size distribution retrieved from error free $3\beta + 2\alpha$ data set is shown in Figure 9. Figure 9 shows model PSD_{10} used to generate the data set. The retrieved size distribution is close to the model one: the error of the total particle volume V estimation is less than 5%. The model value of refractive index is m = 1.55−i0.001 while the retrieved one is m = 1.57−i0.001. Figure 9 shows also the retrieval result when the particles are assumed to be spherical. The error of the total volume estimation in this case is about 48%, which is higher than for spheroidal kernels, still it is better accuracy than we could expect basing on the results shown in Figures 4–6. Moreover, the main features of the model distribution are also reproduced. The highest error occurs in *m* estimation: retrieved refractive index is m = 1.43−i0.004, thus the real part is significantly underestimated, while the imaginary part is usually overestimated (especially when low model values of m_I are tested). Finally, when the exact value of model refractive index is used, the retrieval with spherical kernels fails: the coarse mode of PSD is not reproduced properly.

[30] Relatively small errors of volume estimation with spherical kernels can be understood by comparing the kernels K_β^{ns} and K_β^{s} calculated for different m_R and m_I. For every value of the real part of refractive index $K_\beta^{ns} < K_\beta^{s}$, however backscattering by spheres decreases rapidly with m_R and in some radii range the spheroidal kernels at m_R = 1.55 become comparable to spherical kernels with lower value of m_R. For example, for radii in the interval 0.1–0.5 μm and m_I = 0.001, K_β^{s} (m_R = 1.43) is close to K_β^{ns} (m_R = 1.55). Thus for spheroidal backscattering kernel under consideration it is possible to find spherical one with lower m_R and higher m_I, such that the kernels will be comparable inside the inversion interval. This implies that when the spherical kernels are used for retrieval of dust particles it is possible, that the algorithm may provide reasonable values for particle size and volume, while yielding a refractive index with significant error: the real part m_R will be underestimated, while the imaginary part m_I overestimated.

[31] As already mentioned in section 2.1, the inverse problem in our formulation is underdetermined: the set of lidar measurements within a single atmospheric layer is extremely limited: only 5 observations. Unfortunately, this is not sufficient to uniquely describe the properties of the

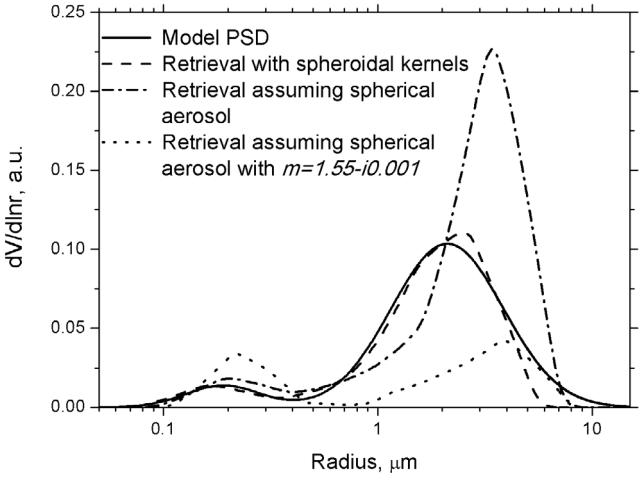

Figure 9. The retrieval of spheroids size distribution with spheroidal and spherical kernels. Dotted line shows the retrieval with spherical kernels when exact value of refractive index is used.

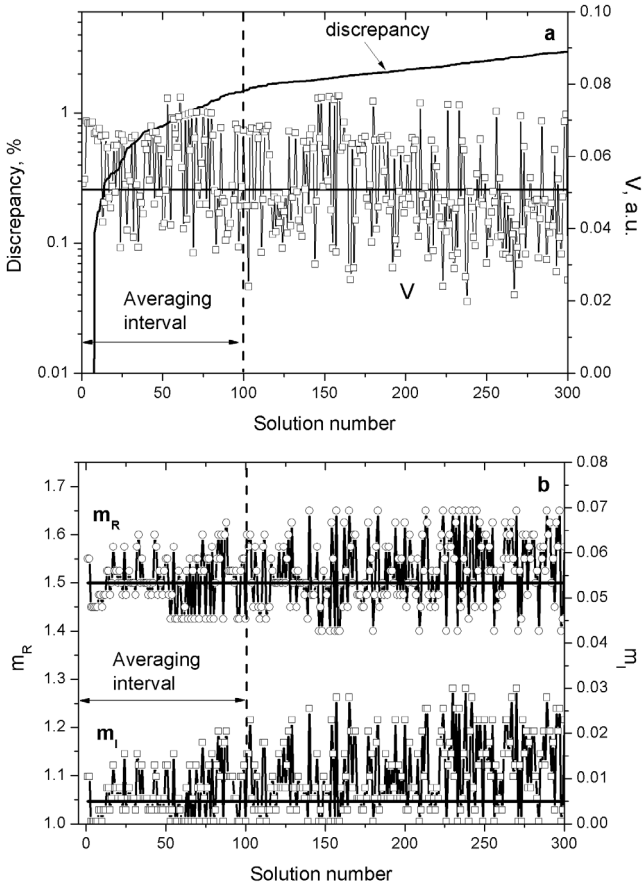

Figure 10. (a) Discrepancy and volume and (b) the real and imaginary part of the refractive index as a function of solution number for the first 300 solutions. Vertical dashed line shows the averaging interval used in the retrieval. Horizontal solid lines correspond the model parameters. Total number of considered solutions is 10^4.

aerosol within the atmospheric layer. Therefore, we use an intermediate approach. We fit the observation and identify not a unique solution but a family of solutions instead. At the same time, in this process of identifying a family of solutions we use a priori constraints, specifically, we limit the range of considered values of refractive index. Although those constraints do not provide uniqueness of the solution they help to significantly reduce the number of solution family members. Once the solution family is identified the results are averaged and the mean solution is provided.

[32] To illustrate the operation of the algorithm, Figure 10 presents particle parameters, such as volume and complex refractive index derived from individual solutions together with their discrepancies. The error free optical data in this retrieval were generated from PSD_{10} with m = 1.5−i.005. The solutions are ranged in accordance with their discrepancy from small to large and the results are shown for the first 300 solutions (the total number of solutions is about 10^4). The retrieved parameters oscillate around the model values, shown by horizontal solid lines. In our retrieval we usually average about 1% of the total number of solutions. The averaging interval is shown by vertical dashed lines. After averaging, the error in the estimation of volume V is less than 5%. The results present no strong sensitivity to the choice of averaging interval.

3.2.2. Effect of Spectrally Dependent Refractive Index

[33] Analyzing the forward problem in section 3.1, we neglected the spectral dependence of the particle refractive index, which can be an additional source of uncertainty in the retrievals. The spectral dependence of refractive index of dust particles components has been reported in numerous laboratory studies from the UV to IR spectral region [*Sokolik and Toon*, 1999]. In situ measurements of imaginary part of mineral dust refractive index in a wide spectral range was performed from the aircraft during SAMUM-1 campaign [*Müller et al.*, 2008]. A significant amount of information on $m(\lambda)$ dependence for dust particles in natural environment in different regions has also been accumulated from AERONET measurements [*Dubovik et al.*, 2002b]. Usually the real part of the refractive index m_R is approximated as constant in 355–1064 nm spectral range, while the imaginary part varies significantly. Figure 11 shows the spectral dependence of m_I used in our model: $m_I = 0.001$ is constant in 650–1064 nm range, but for shorter wavelengths it increases reaching $m_I = 0.0058$ at 355 nm. This model agrees with AERONET observation [*Dubovik et al.*, 2002b; *Eck et al.*, 2005] and with results published by *Sinyuk et al.* [2003].

[34] Figure 11 presents the spectral dependence of spheroidal backscattering coefficients β^{ns} computed from PSD_{10} for spectrally variable m_I and for a fixed value of $m_I = 0.0016$. The real part of the refractive index is $m_R = 1.55$ in both cases. The spectral variation of m_I has an influence only on the backscattering at short wavelengths. To estimate corresponding uncertainties in the retrieval, the optical data were generated using spectrally dependent m_I, while in the retrieval m_I was assumed to be spectrally independent. The retrieval results for PSD_{10} are given in Figure 12. Ignoring the spectral dependence of m_I leads to 17% error in the particle volume estimation. The retrieved refractive index is m = 1.55−i0.003, thus algorithm provides mean over spectrum value of m_I. It should be noted that for big particles the

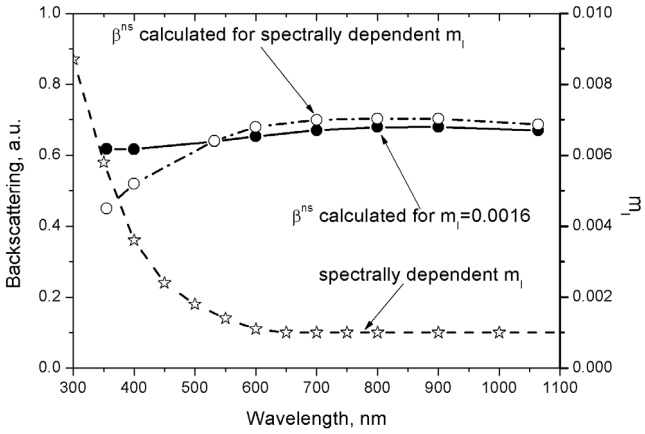

Figure 11. The spectral dependence of spheroids backscattering coefficients calculated for spectrally variable m_I (open circles) and for constant value $m_I = 0.0016$ (solid circles); Calculations were performed for PSD_{10} with $m_R = 1.55$ in both cases. Model spectral dependence of m_I is given by stars.

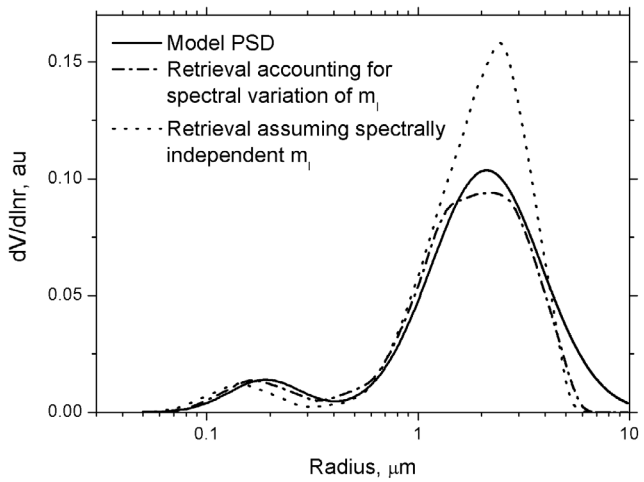

Figure 12. Retrieval of spheroids size distribution assuming spectrally independent m_I and accounting for spectral dependence of m_I.

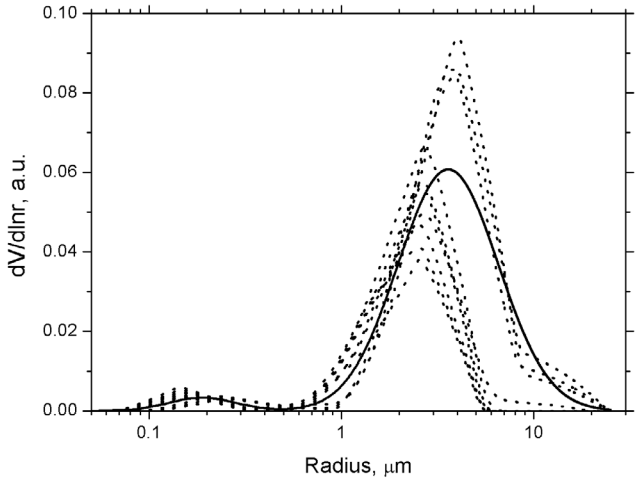

Figure 13. Particle size distributions obtained in 10 runs of retrieval procedure. The 10% errors were introduced in $3\beta + 2\alpha$ optical data in a random way. Solid line shows the model distribution PSD_{20}.

rise of imaginary part at 355 nm provides stronger effect to backscattering. As a result the error of the total volume retrieval for PSD_{20} is enhanced up to 25%.

[35] The uncertainty induced by the spectral dependence of the refractive index is not so high; moreover it can be partly corrected. One of the simplest ways to account for dependence $m_I(\lambda)$ is as follows. Every value of the imaginary part m_I, for which equation (11) is solved, is prescribed at 532 nm, while values of m_I at 355 nm and 1064 nm are calculated using the ratios $\frac{m_I(532nm)}{m_I(355nm)}$, $\frac{m_I(532nm)}{m_I(1064nm)}$ from the model given in Figure 11, assuming that these ratios do not depend on the chosen m_I (532 *nm*). The dust particles are characterized by high value of m_R, so dependence $m_I(\lambda)$ is considered only for $m_R > 1.5$.

[36] The result of such correction is also shown in Figure 12. The error of the total volume retrieval is decreased to 7%. The retrieved refractive index at 532 nm is m = 1.56 −i0.002. which is close to the model value m = 1.55−i0.0016. Such a correction scheme appears to account for the spectral variation of the refractive index. In real dust, the effect of the refractive index on retrieval can be more complicated, including size dependence (refractive indices of the fine and the coarse mode may differ) and dependence on particle shape (spherical and nonspherical fractions may represent the particles of different origin). To introduce corresponding corrections an appropriate model should be chosen, however, the analysis of possible model choices and their implementation in our inversion procedure is beyond the scope of this paper.

3.2.3. Impact of Noise

[37] The uncertainty of parameters retrieval is very sensitive to the presence of the errors in input optical data. The Raman and HSRL techniques are able to provide aerosol backscattering and extinction coefficients with accuracy about 10% and particle depolarization ratio can also be measured with comparable accuracy. To estimate the uncertainty of particle parameters estimation, errors in the range of $0 < \varepsilon < \varepsilon_{max}$ were introduced in the optical data in a random way and the retrieval procedure was repeated a large number of times. The retrieval becomes especially sensitive to input errors for big particle radii, so modeling was performed for both PSD_{10} and PSD_{20}. The high sensitivity of the coarse mode retrieval to the input errors is illustrated by Figure 13, showing PSD_{20} obtained in 10 trials for 10% input errors. Retrieval of the fine mode is quite stable, but scattering of solutions for $r > 5$ μm becomes high.

[38] The results of simulations for ε_{max} = 10% and 20% are summarized in Table 2. Retrieval of PSD_{10} total volume and effective radius for 10% input errors in 90% of the cases can be performed with accuracy better than 30%, while uncertainty of number density estimation is as high as 60%. Increase of particle radii enhances the uncertainty of PSD_{20} volume and effective radius estimation, but it is still less than 45%. The most stable parameter in retrieval is surface density; corresponding uncertainty is about 12% for both distributions. The increase of ε_{max} from 10% to 20% approximately doubles the retrieval uncertainty. Estimation of the real part of refractive index is possible with accuracy better than ±0.04 for ε_{max} = 10%. The most challenging is the estimation of the imaginary part of refractive index. For $m_I > 0.005$ we can do it with 50% accuracy for both distributions. When m_I is below 0.005 we can estimate just upper boundary of imaginary part.

3.2.4. Use of Particle Depolarization Ratios as an Additional Input Optical Data

[39] Multiwavelength lidar based on a tripled Nd:YAG laser is in principle able to provide up to three depolarization ratios at different wavelengths. However, in the retrievals presented in section 3.2.3 we did not show the results obtained with depolarization ratio included in the input data

Table 2. Uncertainties of Estimation of Total Volume (V), Surface (S), Number (N) Density, Effective Radius (r_{eff}), and Real Part of Refractive Index (m_R) for Different PSDs When 10% and 20% Errors are Introduced in the Input Optical Data

Size Distribution	V (%)	S (%)	N (%)	r_{eff} (%)	m_R
PSD_{10}, 10%	25	12	60	30	±0.04
PSD_{10}, 20%	50	25	110	60	±0.05
PSD_{20}, 10%	40	12	80	45	±0.04

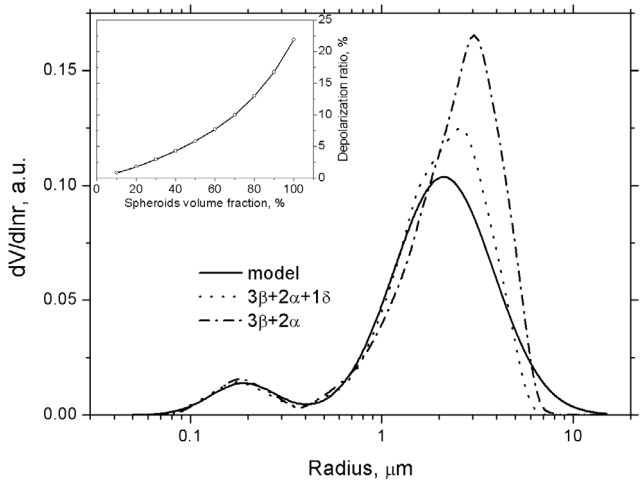

Figure 14. Size distributions of spheres-spheroids mixture retrieved from error free $3\beta + 2\alpha + 1\delta$ and $3\beta + 2\alpha$ sets. Solid lime shows model distribution PSD_{10}. The insert gives particle depolarization at 355 nm as a function of spheroids volume fraction for m = 1.55−i0.005.

set. When the volume fraction of spheroids in model distribution is $\eta = 100\%$ (i.e., spheres are absent) the results obtained from $3\beta + 2\alpha + 1\delta$ set are close to the results obtained in the absence of depolarization ($3\beta + 2\alpha$ set) and no significant improvement was observed. It is not surprising, as the kernels for particle cross-polarized backscattering and for extinction are very similar, as it follows from Figures 1 and 3. However, the depolarization ratio becomes important when the model particles are mixture of spheres and spheroids. Such a model describes the situation when, for example, desert particles are transported over a long range and during transportation are mixed with other types of aerosol (oceanic, biomass burning), and modified potentially by chemical and humidification processes. As a result, a significant part of the particles can be represented by spheres. The spheres provide almost twice as large backscatter as spheroids, as it follows from Figure 4, thus the contribution of irregular particles (spheroidal fraction) can be "masked."

[40] The particle depolarization ratio is a parameter sensitive to the presence of irregular particles [*Tesche et al.*, 2009b]. The importance of using depolarization in retrieval is illustrated by Figure 14. Figure 14 shows the model distribution PSD_{10} and the retrievals obtained from error free $3\beta + 2\alpha + 1\delta$ and $3\beta + 2\alpha$ sets computed for m = 1.55 –i0.005 and spheroids volume fraction $\eta = 60\%$; the depolarization ratio is taken at $\lambda = 355$ nm. The insert in Figure 14 gives the depolarization as a function of spheroids volume fraction, δ_{355} increases monotonically with η reaching maximal value of 23.5%. The PSD retrieved from $3\beta + 2\alpha + 1\delta$ is close to the model and the error of total volume estimation is less than 5%. However, for $3\beta + 2\alpha$ set this error increases up to 25% and retrieved refractive index m = 1.51−i0.007 differs from the model one. The reason for such difference can be understood from Figure 15, showing the structure of solutions. The spheroids volume fraction retrieved from $3\beta + 2\alpha + 1\delta$ and $3\beta + 2\alpha$ sets is plotted as a function of the solution number. The averaging interval comprises 100 solutions with lowest discrepancy, which is about 1% of the total solutions number. For the $3\beta + 2\alpha + 1\delta$ set the retrieved volume fraction η is stable and coincides with the model for all solutions shown. In the absence of depolarization the retrieved η oscillates and the averaged value $\eta = 35\%$ is lower than the model one. The oscillation of η affects the m_R retrieval and as it was pointed previously, the volume estimation.

[41] Numerous runs of the program with 10% randomly introduced errors for the model mixture were performed just as described above. From the results obtained we can conclude that for the $3\beta + 2\alpha + 1\delta$ set the uncertainties of the retrieval of spheres-spheroids mixture parameters are essentially the same as obtained previously for spheroids.

[42] The use of more than one depolarization ratio should farther stabilize the retrieval. Moreover, depolarization ratios can be used instead extinction in retrieval. The simulation shows that $3\beta + 3\delta$ set in principle can provide the estimation of particle volume and refractive index. However, should be kept in mind that a spheroidal model matches quite well the total backscattering of real dust particles though the discrepancies in the calculation of the depolarization ratio may be higher. For example, in Figure 8 from *Dubovik et al.* [2006], there is a notable differences between the ratio of scattering matrix elements P22/P11 derived from experimental data of *Volten et al.* [2001], and calculations performed with a spheroidal model. To understand how accurately the spheroidal model can reproduce the depolarization of backscatter from real dust, more laboratory measurements at scattering angles close to 180 deg performed for different types of dust are needed. To our knowledge no experimental data of this kind are available at a present.

4. Application to Experimental Data

[43] The algorithm described here was applied to the lidar measurements carried out by the Raman lidar system BASIL [*Di Girolamo et al.*, 2009a, 2009b]. The lidar was operational

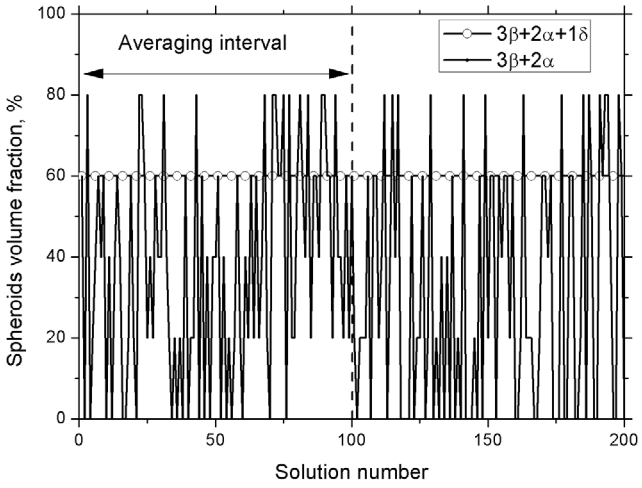

Figure 15. The volume fraction of spheroids η as a function of the solution number for the first 200 solutions. The retrievals were performed for errors free $3\delta + 2\alpha + 1\delta$ (circles) and $3\delta + 2\alpha$ (solid lines) data sets. Model value is $\eta = 60\%$; vertical dashed line shows the averaging interval used in the retrieval. Total number of considered solutions is 10^4.

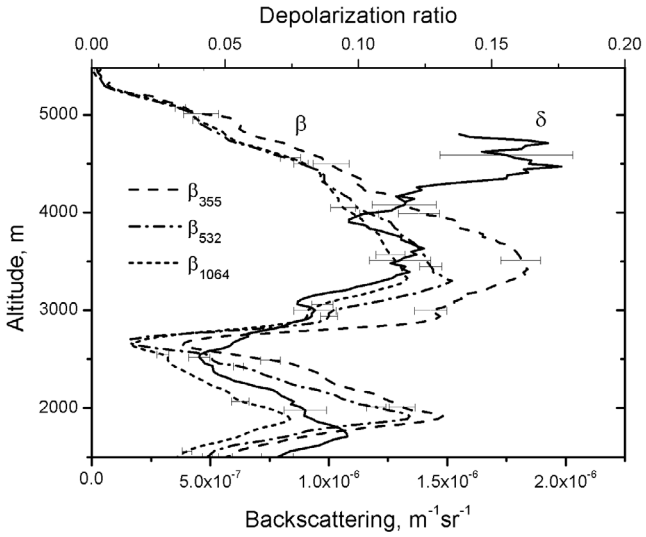

Figure 16. Backscattering (β) at 355, 532, and 1064 nm and depolarization ratio (δ) at 355 nm measured on 2 August 2007.

in Achern (Black Forest) between 25 May and 30 August 2007 in the framework of the Convective and Orographically induced Precipitation Study (COPS) [*Wulfmeyer et al.*, 2008]. The system was able to measure three backscattering coefficients at 355, 532 and 1064 nm, two extinction coefficients at 355 and 532 nm, and depolarization at 355 nm. Here we consider the data for 2 August in the time interval 0000–0030 UTC and in the height interval 3500–3900 m to illustrate the main features of the algorithm operation. On this day a Saharan dust outbreak event was observed. Lidar data clearly reveal the presence of the dust cloud between 1800 and 0300 UTC, with the presence of two almost separate aerosol layers: a lower layer located between 1.5 and 3.5 km and an upper layer extending between 3.0 and 6.0 km. Figure 16 shows the vertical profiles of the backscattering coefficient and the particle depolarization ratio on 2 August. The lidar ratios did not change much with height, the averaged in 3000–4500 m height interval value is 68 ± 10 sr for 355 nm and 58 ± 8 sr for 532 nm wavelengths, which is typical for desert dust. Particle depolarization ratio in these measurements did not exceed 15%, thus pointing that the aerosol should contain significant amount of spherical particles.

[44] To illustrate the algorithm operation we have chosen the height layer 3500–3900 m, which is right in the middle of the upper dust layer. The lidar data for this height interval, such as lidar ratios, Angstrom extinction and backscattering exponents are summarized in Table 3. The Angstrom extinction exponent at 355–532 nm is about 0.6, which indicates the presence of significant volume fraction of small particles. The results of retrievals are shown in Figures 17–19. In the retrieval the real part of refractive index was varied over the range 1.35–1.65 with a step size of 0.025, while the imaginary part varied over the range 0–0.015 with the step size of 0.001, η varied from 0 to 100% with step size 20%. The solutions were ordered in accordance with their discrepancy from smallest discrepancy to largest discrepancy. As mentioned in section 2, the inverse

Table 3. Measured Lidar Ratio (LR), Extinction (k^{α}), and Backscattering (k^{β}) Angstrom Exponents for the Height Layer 3500–3900 m

LR_{355}, sr	LR_{532}, sr	$k^{\alpha}_{355-532}$	$k^{\beta}_{355-532}$	$k^{\beta}_{532-1064}$	$\delta_{355,\ \%}$
65 ± 10	62 ± 9	0.62 ± 0.15	0.53 ± 0.15	0.25 ± 0.15	11.5 ± 2

problem in our case is underdetermined: we solve the system of equation (11) for a large set of m and η. So there is a probability, that the solutions with small discrepancy will be obtained for particle parameters varying in a very large range, thus we will not be able to get particle parameters with acceptable accuracy. To test for this condition we perform analysis of obtained solutions. Figure 17 shows discrepancy of individual solutions f_i as a function of solution number i. Normally we average 1% of solutions, but as it follows from Figure 17, the retrieved values of spheroids fraction, volume, surface density depend weakly on the chosen averaging interval. Irregular particles in this layer are responsible for 80% of the total particles volume. In accordance with our simulations, the most stable parameter

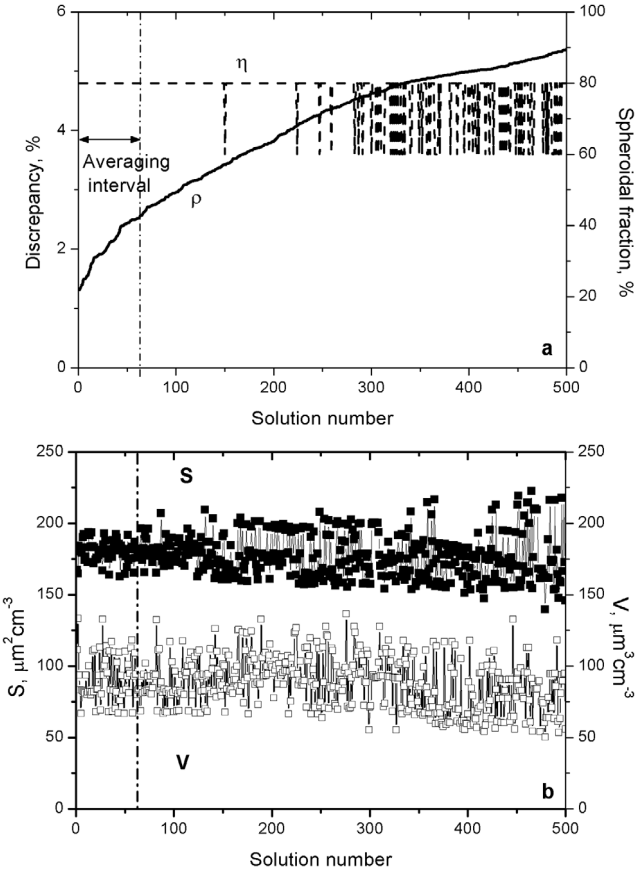

Figure 17. (a) Discrepancy ρ of individual solutions, spheroidal volume fraction η and (b) surface S and volume V density derived from individual solutions as a function of solution number in 3500–3900 m height layer. Vertical dash-dotted lines show the averaging interval used in the retrieval. Total number of considered solutions is about 7000.

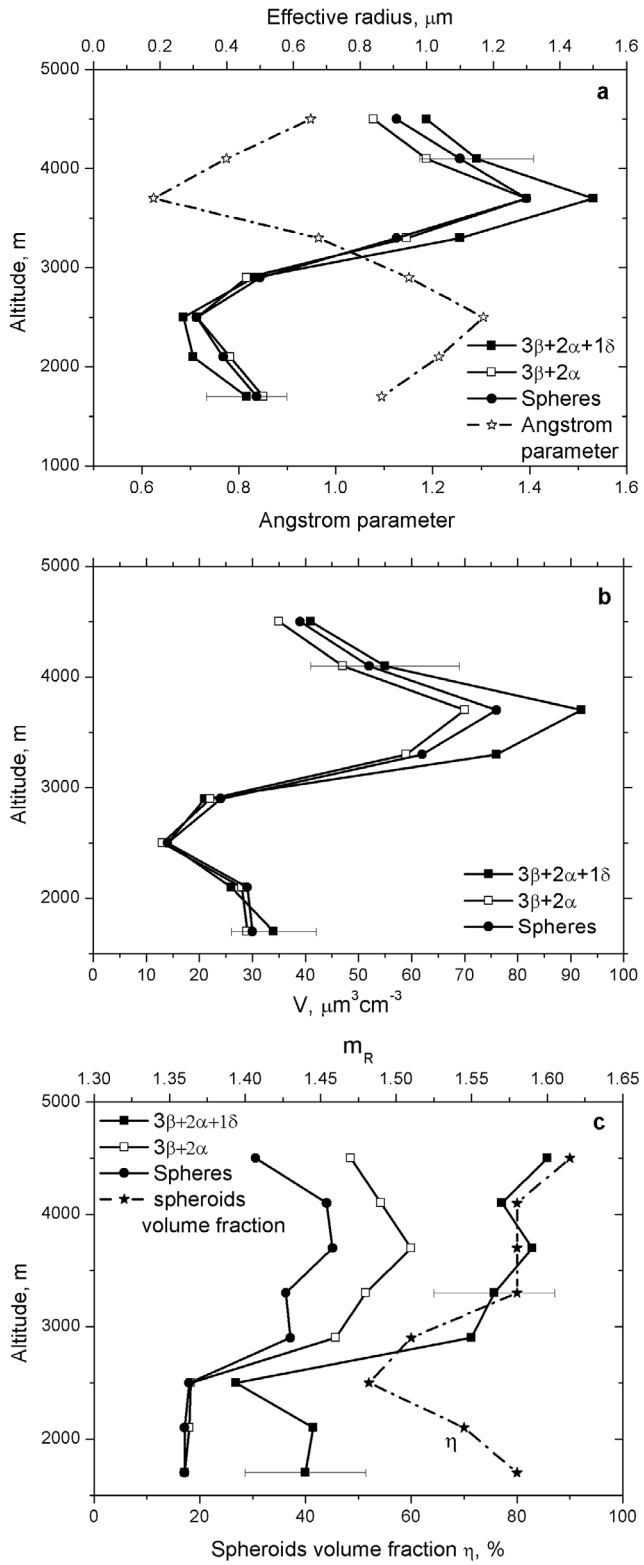

Figure 18. Vertical profiles of particle (a) effective radius and Angstrom parameter at 355–532 nm, (b) volume density, and (c) real part of refractive index and spheroids volume fraction η. Retrieval was performed from $3\beta + 2\alpha + 1\delta$ (solid squares) and $3\beta + 2\alpha$ (open squares) sets and assuming spherical aerosol (circles).

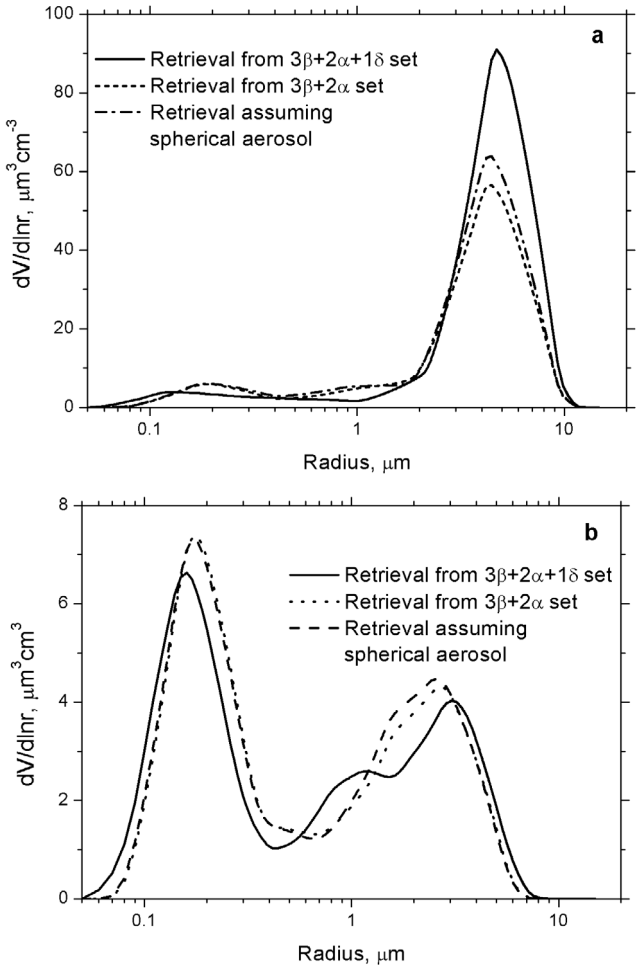

Figure 19. The PSDs at (a) 3700 m and (b) 2500 m on 2 August retrieved from complete data set ($3\beta + 2\alpha + 1\delta$), from data set without depolarization ratio ($3\beta + 2\alpha$) and PSD retrieved in the assumption of spherical aerosol.

in retrieval is surface density S, it is characterized by the lowest standard deviation SD of values derived from individual solutions: inside the averaging interval the ratio of standard deviation to mean value $\frac{SD}{S_{mean}} = 4\%$, while for volume corresponding value is 17%. It should be noted, that the actual uncertainty of the parameters retrieval could be higher than the standard deviation, because the mean values of the derived parameters show only the mean of the identified solution family and the standard deviation shows a spread of these solutions. At the same time, both the mean of the solutions and their spread may also strongly depend on the error distribution in the input data. Therefore for uncertainties we use the values obtained in numerical simulation described in Table 2.

[45] The vertical profiles of particle volume, effective radius and real part of refractive index are shown in Figure 18. Retrieval was performed from $3\beta + 2\alpha + 1\delta$ and $3\beta + 2\alpha$ sets; Figure 18 also shows the results obtained with the spherical kernels. Effective radius reaches the maximal value of 1.5 μm in the height layer centered at 3700 m, in the same layer the highest particle volume density 92 $\mu m^3/cm^3$ occurs. The smallest effective radius 0.27 μm is observed at 2500 m,

this layer is characterized by lowest depolarization ratio of 5%. Retrieved height profile of effective radius correlates with profile of Angstrom parameter, obtained from extinctions at 355 and 532 nm, as it shown in Figure 18a. Maximal value of effective radius corresponds to the minimal value of Angstrom parameter, thus the retrieved height profile of r_{eff} looks reasonable. The real part of refractive index rises with height from 1.44 at 1700 m to 1.57 in the upper dust layer. The imaginary part of refractive was 0.006 ± 0.003 and inside this uncertainty in did not demonstrate significant height variation.

[46] Figure 18c shows the vertical profile of retrieved spheroid volume fraction η, which should quantify the fraction of volume attributed to nonspherical particles. The lowest and highest values of η obtained in retrievals are 50% and 90%. For low values of η the particles parameters obtained from $3\beta + 2\alpha + 1\delta$, $3\beta + 2\alpha$ sets and parameters retrieved with spherical kernels are close, however for 2900–4500 m height range where η rises up to 90% the difference becomes noticeable. Thus at 3700 m the particle volume retrieved with ($3\beta + 2\alpha + 1\delta$ set) and without spheroids is 92 and 76 $\mu m^3/cm^3$. Excluding of depolarization ratio from data set also leads to almost 25% decrease of particle volume, because without depolarization data the spheroidal fraction η is underestimated. The real parts of refractive index obtained with all three approaches tend to become close at 2900 m where volume fraction of nonspherical particles is low, but for η = 80% the difference becomes significant: m_R = 1.57 and 1.45 when retrieval is performed with and without spheroids. The underestimation of m_R in retrieval with spherical kernels is expected from simulation results presented in section 3. The height variation of η correlates with changes of depolarization. From Figures 16 and 18 we can conclude, that for particle depolarization exceeding ~10% the use of spheroidal kernels becomes essential.

[47] The height variation of Angstrom parameter observed in the measurements is caused by variation of PSD. Figure 19 shows the size distributions for 3500–3900 m and 2300–2700 m height layers, corresponding the lowest (in the center of the dust layer) and the highest (outside of the dust layer) values of Angstrom parameter. Again three approaches are considered: retrieval from $3\beta + 2\alpha + 1\delta$, $3\beta + 2\alpha$ set and retrieval using spherical kernels only. At 3700 m the coarse mode is centered at r = 5 μm and it dominates in $\frac{dV}{d\ln r}$ distribution. Such size distribution is quite typical for the desert dust aerosol [*Dubovik et al.*, 2002b]. The use of only spherical kernels, as well as ignoring depolarization ratio, underestimates the coarse mode. In the size distribution retrieved at 2500 m, which is outside of the main dust layer, the fine mode prevails, and the results obtained with all three approaches are close. The presented experimental case demonstrates the importance of using spheroids kernels for the retrieval of parameters of desert dust particles.

5. Conclusions

[48] We described an algorithm based on the model of polydisperse, randomly oriented spheroids for the retrieval of parameters of dust particles from multiwavelength lidar measurements. Numerical simulations demonstrate that for typical dust PSDs a Raman lidar based on a tripled Nd:YAG laser is able to estimate particle parameters such as surface, volume density, and particle effective radius with accuracy better than 30%. After having compared retrievals performed with sphere-based and spheroid-based kernels, we can conclude that the application of spheres to the retrieval of dust particles will in general lead to an underestimation of the real part of the refractive index, as a result the uncertainty in the retrieval of other parameters is also increased. Still in many cases the sphere-based kernels allow a reasonable estimation of the dust particle size and volume.

[49] The algorithm developed allows one to use the particle depolarization ratio at multiple wavelengths as an additional input data in the inversion. The use of at least one depolarization becomes essential when a significant fraction of the particle population is represented by nearly spherical particles. Without the use of depolarization the algorithm yields incorrect values of the spheroidal particle volume fraction and thus the uncertainty of particle parameters estimation is increased.

[50] An initial attempt to apply our algorithm incorporating spheroid-based kernels to experimental data obtained with the BASIL multiwavelength Raman lidar was presented. It was shown that the algorithm developed provided substantially reasonable results. Comparisons of the results obtained in the framework of our spheroid particle model with the results derived assuming spherical particles demonstrates that for particle depolarization ratios exceeding 10% the use of spheroids becomes essential.

[51] On the other hand, our approach employs several fundamental assumptions. For example, the complex refractive index, the spheroid aspect ratio, and the volume fraction of spheroidal particles were assumed to be size independent. Therefore, performing additional tests by means of both numerical simulations and comparisons with independent experimental results is highly desirable in order to validate this technique. Further work on algorithm improvement is in progress.

References

Ansmann, A., M. Riebesell, U. Wandinger, C. Weitkamp, E. Voss, W. Lahmann, and W. Michaelis (1992), Combined Raman elastic-backscatter lidar for vertical profiling of moisture, aerosols extinction, backscatter, and lidar ratio, *Appl. Phys. B*, *55*, 18–28, doi:10.1007/BF00348608.

Ansmann, A., M. Tesche, P. Knippertz, E. Bierwirth, D. Althausen, D. Muller, and O. Schultz (2009), Vertical profiling of convective dust plumes in southern Morocco during SAMUM, *Tellus, Ser. B*, *61*, 340–353.

Bohren, C. F., and D. R. Huffman (1983), *Absorption and Scattering of Light by Small Particles*, 530 pp., John Wiley, Hoboken, N. J.

Bohren, C. F., and S. B. Singham (1991), Backscattering by nonspherical particles–a review of methods and suggested new approaches, *J. Geophys. Res.*, *96*, 5269–5277, doi:10.1029/90JD01138.

Bond, T. C., M. Bussemer, B. Wehner, S. Keller, R. J. Charlson, and J. Heintzenberg (1999), Light absorption by primary particle emissions from a lignite burning plant, *Environ. Sci. Technol.*, *33*, 3887–3891, doi:10.1021/es9810538.

Cattrall, C., J. Reagan, K. Thome, and O. Dubovik (2005), Variability of aerosol and spectral lidar and backscatter and extinction ratios of key aerosol types derived from selected Aerosol Robotic Network locations, *J. Geophys. Res.*, *110*, D10S11, doi:10.1029/2004JD005124.

De Tomasi, F., A. Bianco, and M. R. Perrone (2003), Raman lidar monitoring of extinction and backscattering of African dust layers and dust characterization, *Appl. Opt.*, *42*, 1699–1709, doi:10.1364/AO.42.001699.

Di Girolamo, P., D. Summa, and R. Ferretti (2009a), Rotational Raman lidar measurements for the characterization of stratosphere-troposphere exchange mechanisms, *J. Atmos. Oceanic Technol.*, *26*, 1742–1762, doi:10.1175/2009JTECHA1253.1.

Di Girolamo, P., D. Summa, R. F. Lin, T. Maestri, R. Rizzi, and G. Masiello (2009b), UV Raman lidar measurements of relative humidity for the characterization of cirrus cloud microphysical properties, *Atmos. Chem. Phys.*, *9*, 8799–8811, doi:10.5194/acp-9-8799-2009.

Draine, B. T., and J. P. Flatau (1994), Discrete-dipole approximation for scattering calculations, *J. Opt. Soc. Am. A Opt. Image Sci. Vis.*, *11*, 1491–1499, doi:10.1364/JOSAA.11.001491.

Dubovik, O., and M. D. King (2000), A flexible inversion algorithm for retrieval of aerosol optical properties from Sun and sky radiance measurements, *J. Geophys. Res.*, *105*, 20,673–20,696, doi:10.1029/2000JD900282.

Dubovik, O., A. Smirnov, B. N. Holben, M. D. King, Y. J. Kaufman, T. F. Eck, and I. Slutsker (2000), Accuracy assessments of aerosol optical properties retrieved from AERONET Sun and sky radiance measurements, *J. Geophys. Res.*, *105*, 9791–9806, doi:10.1029/2000JD900040.

Dubovik, O., B. N. Holben, T. Lapyonok, A. Sinyuk, M. I. Mishchenko, P. Yang, and I. Slutsker (2002a), Non-spherical aerosol retrieval method employing light scattering by spheroids, *Geophys. Res. Lett.*, *29*(10), 1415, doi:10.1029/2001GL014506.

Dubovik, O., B. Holben, T. F. Eck, A. Smirnov, Y. J. Kaufman, M. D. King, D. Tanré, and I. Slutsker (2002b), Variability of absorption and optical properties of key aerosol types observed in worldwide locations, *J. Atmos. Sci.*, *59*, 590–608, doi:10.1175/1520-0469(2002)059<0590:VOAAOP>2.0.CO;2.

Dubovik, O., et al. (2006), Application of spheroid models to account for aerosol particle nonsphericity in remote sensing of desert dust, *J. Geophys. Res.*, *111*, D11208, doi:10.1029/2005JD006619.

Eck, T. F., et al. (2005), Columnar aerosol optical properties at AERONET sites in central eastern Asia and aerosol transport to the tropical mid-Pacific, *J. Geophys. Res.*, *110*, D06202, doi:10.1029/2004JD005274.

Esselborn, M., M. Wirth, A. Fix, B. Weinzierl, K. Rasp, M. Tesche, and A. Petzold (2009), Spatial distribution and optical properties of Saharan dust observed by airborne high spectral resolution lidar during SAMUM 2006, *Tellus, Ser. B*, *61*, 131–143.

Freudenthaler, V., et al. (2009), Depolarization ratio profiling at several wavelengths in pure Saharan dust during SAMUM 2006, *Tellus, Ser. B*, *61*, 165–179.

Gérard, B., J. L. Déuze, M. Herman, Y. J. Kaufman, P. Lallart, C. Oudard, L. A. Remer, B. Roger, B. Six, and D. Tanré (2005), Comparisons between POLDER 2 and MODIS/Terra aerosol retrievals over ocean, *J. Geophys. Res.*, *110*, D24211, doi:10.1029/2005JD006218.

Govaerts, Y. M., S. Wagner, A. Lattanzio, and P. Watts (2010), Joint retrieval of surface reflectance and aerosol optical depth from MSG/SEVIRI observations with an optimal estimation approach: 1. Theory, *J. Geophys. Res.*, *115*, D02203, doi:10.1029/2009JD011779.

Haywood, J., P. Francis, S. Osborne, M. Glew, N. Loeb, E. Highwood, D. Tanré, G. Myhre, P. Formenti, and E. Hirst (2003), Radiative properties and direct radiative effect of Saharan dust measured by the C-130 aircraft during SHADE: 1. Solar spectrum, *J. Geophys. Res.*, *108*(D18), 8577, doi:10.1029/2002JD002687.

Heese, B., D. Althausen, T. Dinter, M. Esselborn, T. Muller, M. Tesche, and M. Wiegner (2009), Vertically resolved dust optical properties during SAMUM: Tinfou compared to Ouarzazate, *Tellus, Ser. B*, *61*, 195–205.

Heintzenberg, J. (2009), The SAMUM-1 experiment over Southern Morocco: Overview and introduction, *Tellus, Ser. B*, *61*, 2–11.

Holben, B. N., et al. (1998), AERONET—A federated instrument network and data archive for aerosol characterization, *Remote Sens. Environ.*, *66*, 1–16, doi:10.1016/S0034-4257(98)00031-5.

Kahnert, M. (2004), Reproducing the optical properties of fine desert dust aerosols using ensembles of simple model particles, *J. Quant. Spectrosc. Radiat. Transfer*, *85*, 231–249, doi:10.1016/S0022-4073(03)00227-9.

Levy, R., L. Remer, and O. Dubovik (2007), Global aerosol optical models and application to MODIS aerosol retrieval over land, *J. Geophys. Res.*, *112*, D13210, doi:10.1029/2006JD007815.

Li, Z., et al. (2009), Improvements for ground-based remote sensing of atmospheric aerosol properties by additional polarimetric measurements, *J. Quant. Spectrosc. Radiat. Transfer*, *110*, 1954–1961, doi:10.1016/j.jqsrt.2009.04.009.

Liu, Z., N. Sugimoto, and T. Murayama (2002), Extinction-to-backscatter ratio of Asian dust observed with high-spectral-resolution lidar and Raman lidar, *Appl. Opt.*, *41*, 2760–2767, doi:10.1364/AO.41.002760.

Liu, Z., et al. (2008), CALIPSO lidar observations of the optical properties of Saharan dust: A case study of long-range transport, *J. Geophys. Res.*, *113*, D07207, doi:10.1029/2007JD008878.

Mattis, I., A. Ansmann, D. Müller, U. Wandinger, and D. Althausen (2002), Dual-wavelength Raman lidar observations of the extinction-to-backscatter ratio of Saharan dust, *Geophys. Res. Lett.*, *29*(9), 1306, doi:10.1029/2002GL014721.

Min, M., J. W. Hovenier, and A. de Koter (2005), Modeling optical properties of cosmic dust grains using a distribution of hollow spheres, *Astron. Astrophys.*, *432*, 909–920, doi:10.1051/0004-6361:20041920.

Mishchenko, M. I., and L. D. Travis (1994), *T*-matrix computations of light scattering by large spheroidal particles, *Opt. Commun.*, *109*, 16–21, doi:10.1016/0030-4018(94)90731-5.

Mishchenko, M. I., A. A. Lacis, B. E. Carlson, and L. D. Travis (1995), Nonsphericity of dust-like tropospheric aerosols: Implications for aerosol remote sensing and climate modeling, *Geophys. Res. Lett.*, *22*, 1077–1080, doi:10.1029/95GL00798.

Mishchenko, M. I., L. D. Travis, R. A. Kahn, and R. A. West (1997), Modeling phase functions for dustlike tropospheric aerosols using a mixture of randomly oriented polydisperse spheroids, *J. Geophys. Res.*, *102*, 16,831–16,847, doi:10.1029/96JD02110.

Mishchenko, M. I., J. W. Hovenier, and L. D. Travis (Eds.) (2000), *Light Scattering by Nonspherical Particles*, Academic, San Diego, Calif.

Mishchenko, M. I., L. D. Travis, and A. A. Lacis (2002), *Scattering, Absorption, and Emission of Light by Small Particles*, Cambridge Univ. Press, Cambridge, U. K.

Mona, L., A. Amodeo, M. Pandolfi, and G. Pappalardo (2006), Saharan dust intrusions in the Mediterranean area: Three years of Raman lidar measurements, *J. Geophys. Res.*, *111*, D16203, doi:10.1029/2005JD006569.

Moulin, C., C. E. Lambert, F. Dulac, and U. Dayan (1997), Control of atmospheric export of dust from North Africa by the North Atlantic Oscillation, *Nature*, *387*, 691–694, doi:10.1038/42679.

Müller, D., U. Wandinger, and A. Ansmann (1999), Microphysical particle parameters from extinction and backscatter lidar data by inversion with regularization: Theory, *Appl. Opt.*, *38*, 2346–2357, doi:10.1364/AO.38.002346.

Müller, D., I. Mattis, U. Wandinger, A. Ansmann, D. Althausen, O. Dubovik, S. Eckhardt, and A. Stohl (2003), Saharan dust over a central European EARLINET-AERONET site: Combined observations with Raman lidar and Sun photometer, *J. Geophys. Res.*, *108*(D12), 4345, doi:10.1029/2002JD002918.

Müller, T., A. Schladitz, A. Massling, N. Kaaden, K. Kandler, and A. Wiedensohler (2008), Spectral absorption coefficients and imaginary parts of refractive indices of Saharan dust during SAMUM-1, *Tellus, Ser. B*, *6*, 79–95.

Perrone, M. R., F. Barnaba, F. De Tomasi, G. P. Gobbi, and A. M. Tafuro (2004), Imaginary refractive-index effects on desert-aerosol extinction versus backscatter relationships at 351 nm: Numerical computations and comparison with Raman lidar measurements, *Appl. Opt.*, *43*, 5531–5541, doi:10.1364/AO.43.005531.

Reid, E. A., J. S. Reid, M. M. Meier, M. R. Dunlap, S. S. Cliff, A. Broumas, K. Perry, and H. Maring (2003), Characterization of African dust transported to Puerto Rico by individual particle and size segregated bulk analysis, *J. Geophys. Res.*, *108*(D19), 8591, doi:10.1029/2002JD002935.

Reid, J. S., et al. (2003), Comparison of size and morphological measurements of coarse mode dust particles from Africa, *J. Geophys. Res.*, *108*(D19), 8593, doi:10.1029/2002JD002485.

Sinyuk, A., O. Torres, and O. Dubovik (2003), Combined use of satellite and surface observations to infer the imaginary part of refractive index of Saharan dust, *Geophys. Res. Lett.*, *30*(2), 1081, doi:10.1029/2002GL016189.

Sokolik, I. N., and O. B. Toon (1999), Incorporation of mineralogical composition into models of the radiative properties of mineral aerosol from UV to IR wavelengths, *J. Geophys. Res.*, *104*, 9423–9444, doi:10.1029/1998JD200048.

Sokolik, I. N., D. M. Winker, G. Bergametti, D. A. Gillette, G. Carmichael, Y. J. Kaufman, L. Gomes, L. Schuetz, and J. E. Penner (2001), Introduction to special section: Outstanding problems in quantifying the radiative impacts of mineral dust, *J. Geophys. Res.*, *106*, 18,015–18,027, doi:10.1029/2000JD900498.

Swap, R. S., S. Ulanski, M. Cobbett, and M. Garstang (1996), Temporal and spatial characteristics of Saharan dust outbreaks, *J. Geophys. Res.*, *101*, 4205–4220, doi:10.1029/95JD03236.

Tanré, D., J. Haywood, J. Pelon, J. F. Leon, B. Chatenet, P. Formenti, P. Francis, P. Goloub, E. J. Highwood, and G. Myhre (2003), Measurement and modeling of the Saharan dust radiative impact: Overview of the Saharan Dust Experiment (SHADE), *J. Geophys. Res.*, *108*(D18), 8574, doi:10.1029/2002JD003273.

Tesche, M., et al. (2009a), Vertical profiling of Saharan dust with Raman lidars and airborne HSRL in southern Morocco during SAMUM, *Tellus, Ser. B*, *61*, 144–164.

Tesche, M., A. Ansmann, D. Muller, D. Althausen, R. Engelmann, V. Freudenthaler, and S. Groß (2009b), Vertically resolved separation of dust and smoke over Cape Verde using multiwavelength Raman and polarization lidars during Saharan Mineral Dust Experiment 2008, *J. Geophys. Res.*, *114*, D13202, doi:10.1029/2009JD011862.

Twomey, S. (Ed.) (1977), *Introduction to the Mathematics of Inversion in Remote Sensing and Direct Measurements*, Elsevier, New York.

van de Hulst, H. C. (1957), *Light Scattering by Small Particles*, John Wiley, Hoboken, N. J.

Veselovskii, I., A. Kolgotin, V. Griaznov, D. Müller, U. Wandinger, and D. Whiteman (2002), Inversion with regularization for the retrieval of tropospheric aerosol parameters from multi-wavelength lidar sounding, *Appl. Opt.*, *41*, 3685–3699, doi:10.1364/AO.41.003685.

Veselovskii, I., A. Kolgotin, V. Griaznov, D. Müller, K. Franke, and D. N. Whiteman (2004), Inversion of multi-wavelength Raman lidar data for retrieval of bimodal aerosol size distribution, *Appl. Opt.*, *43*, 1180–1195, doi:10.1364/AO.43.001180.

Veselovskii, I., D. N. Whiteman, A. Kolgotin, E. Andrews, and M. Korenskii (2009), Demonstration of aerosol property profiling by multi-wavelength lidar under varying relative humidity conditions, *J. Atmos. Oceanic Technol.*, *26*, 1543–1557, doi:10.1175/2009JTECHA1254.1.

Volten, H., O. Munoz, E. Rol, J. F de Haan, W. Vassen, J. W. Hovenier, K. Muinonen, and T. Nousiainen (2001), Scattering matrices of mineral aerosol particles at 441.6 nm and 632.8 nm, *J. Geophys. Res.*, *106*, 17,375–17,401, doi:10.1029/2001JD900068.

Wiegner, M., et al. (2009), Numerical simulations of optical properties of Saharan dust aerosols with emphasis on lidar applications, *Tellus, Ser. B*, *61*, 180–194.

Wiscombe, W. J., and A. Mugnai (1986), Single scattering from nonspherical Chebyshev particles, *NASA Ref. Publ.*, *1157*, 284 pp.

Wulfmeyer, V., et al. (2008), The Convective and Orographically induced Precipitation Study: A research and development project of the World Weather Research Program for Improving Quantitative Precipitation Forecasting in Low-mountain Regions, *Bull. Am. Meteorol. Soc.*, *89*(10), 1477–1486, doi:10.1175/2008BAMS2367.1.

Xie, C., T. Nishizawa, N. Sugimoto, I. Matsui, and Z. Wang (2008), Characterization of aerosol optical properties in pollution and Asian dust episodes over Beijing, China, *Appl. Opt.*, *47*, 4945–4951, doi:10.1364/AO.47.004945.

Yang, P., and K. N. Liou (1996), Geometric-optics-integral-equation method for light scattering by nonspherical ice crystals, *Appl. Opt.*, *35*, 6568–6584, doi:10.1364/AO.35.006568.

Yang, P., K. N. Liou, M. I. Mishchenko, and B. C. Gao (2000), Efficient finite-difference time-domain scheme for light scattering by dielectric particles: Application to aerosols, *Appl. Opt.*, *39*, 3727–3737, doi:10.1364/AO.39.003727.

Yang, P., Q. Feng, G. Hong, G. W. Kattawar, W. J. Wiscombe, M. I. Mishchenko, O. Dubovik, I. Laszlo, and I. N. Sokolik (2007), Modeling of the scattering and radiative properties of nonspherical dust-like aerosols, *J. Atmos. Sci.*, *38*(10), 995–1014.

Zhao, T. X.-P., I. Laszlo, O. Dubovik, B. N. Holben, J. Sapper, D. Tanré, and C. Pietras (2003), A study of the effect of non-spherical dust particles on the AVHRR aerosol optical thickness retrievals, *Geophys. Res. Lett.*, *30*(6), 1317, doi:10.1029/2002GL016379.

P. Di Girolamo and D. Summa, DIFA, Università della Basilicata, Viale dell'Ateneo Lucano 10, I-85100 Potenza, Italy. (digirolamo@unibas.it)

O. Dubovik, T. Lapyonok, and D. Tanré, Laboratoire d'Optique Atmospherique, CNRS Universite de Lille 1, Bat P5 Cite scientifique, F-59655 Villeneuve d'Ascq CEDEX, France. (dubovik@loa.univ-lille1.fr)

A. Kolgotin and I. Veselovskii, Physics Instrumentation Center, Troitsk, Moscow Region 142190, Russia. (igorv@pic.troitsk.ru)

M. Mishchenko, NASA Goddard Institute for Space Studies, New York, NY 10025-7886, USA.

D. N. Whiteman, Mesoscale Atmospheric Processes Branch, NASA Goddard Space Flight Center, Greenbelt, MD 20771, USA. (david.n.whiteman@nasa.gov)